Optoelectronic and transport properties of vacancy-ordered double-perovskite halides: A first-principles study

Supriti Ghorui,[1] Jiban Kangsabanik,[1,2] M. Aslam,[1] and Aftab Alam [1,*]

[1]*Department of Physics, Indian Institute of Technology Bombay, Powai, Mumbai 400076, India*
[2]*Department of Physics, Technical University of Denmark, 2800 Kongens Lyngby, Denmark*

In the search for stable lead-free perovskites, vacancy-ordered double perovskites (VODPs), A_2BX_6, have emerged as a promising class of materials for solar harvesting owing to their nontoxicity, better stability, and unique optoelectronic properties. Recently, this class has been explored for a wide range of applications, such as photovoltaics, photodetectors, photocatalysis, and light-emitting diodes. Here, we present the stability and the key physical attributes of a few selected compounds in a systematic manner using state-of-the-art first-principles calculations. A careful structural and stability analysis via simulation of convex hulls and compositional phase diagrams for different structural prototypes discloses 14 stable compounds and one metastable compound in this class. Electronic structure calculations using hybrid functionals reveals that six compounds possess band gaps in the ideal visible region. These six compounds, namely Cs_2SnI_6, Cs_2PdI_6, Cs_2TeI_6, Cs_2TiI_6, Cs_2PtI_6, and Cs_2PdBr_6, show high optical absorption ($\approx 10^5$ cm^{-1}), giving rise to high spectroscopic limited maximum efficiency (15–23%) in the thin-film thickness range. Close inspection of the transport properties reveals polar optical phonon scattering to be the dominant mechanism limiting overall mobility. Further analysis of the polaron excitations discloses the possibility of large polaron formation at low to moderate defect concentrations. At high defect concentrations, ionized impurity scattering takes over. Such analysis can be extremely useful for choosing the optimal growth conditions for a given material intended to be used for a desired application. Additionally, a few selected compounds show moderate to high electron mobility values ($\sim$ 13–63 cm^2 V^{-1} s^{-1}) at room temperature. Overall, the present study paves an important path to help design VODPs as lead-free potential candidates for future optoelectronic applications.

I. INTRODUCTION

Lead halide perovskites have reignited immense research interest in the photovoltaics (PV) community due to their remarkable power conversion efficiency (PCE) of 25.6% [1] (to date) and affordable device processability. The rapid rise in PCE (from 3.8% to 25.6%) in a short period of time (from 2009 to 2021) is attributed to their high absorption coefficient, high charge-carrier mobility, defect tolerance, and cost-effective flexible synthesis. Because of their suitable optoelectronic properties, they have also been explored as photodetectors (PDs) [2, 3], photocatalysts [4,5], and light-emitting diodes (LEDs) [6,7]. Yet, there remain two major challenges in their large-scale scalability: (1) lead (Pb) toxicity and (2) stability in ambient environments. At present, major research efforts at laboratory scale have been devoted to overcome these issues without losing their original PV performance [8–12].

This has led to a detailed exploration of the diverse chemical space of halide perovskites (ABX$_3$) [13] and their derivatives [14–16]. Among these perovskite derivatives, three major stoichiometric classes have garnered immense research interest. One of the classes, namely double perovskites with stoichiometry $A_2BB'X_6$, is mainly generated via transmutation of a combination of trivalent and monovalent elements at B sites [17]. For example, $Cs_2BiAgBr_6$ [17–19], $Cs_2InAgCl_6$ [20], etc. belong to the double-perovskite class, which has been extensively explored for various optoelectronic applications. Similarly, $A_3B_2X_9$ (e.g. $Cs_3Bi_2I_9$ [21], $Cs_3Sb_2I_9$ [22], etc.) and A_2BX_6 (e.g. Cs_2SnI_6 [23], Cs_2TiI_6 [24], etc.) structures are constructed by replacing with trivalent and tetravalent atoms, respectively, and leaving a vacant B site. Here, A_2BX_6 is also called a vacancy-ordered double perovskite (VODP), where corner-shared alternate BX$_6$ octahedra are removed along all three directions from the unit cell, as shown in Fig. 1(a).

In the past few years, the VODP family (A_2BX_6) has gradually drawn significant attention in a wide range of
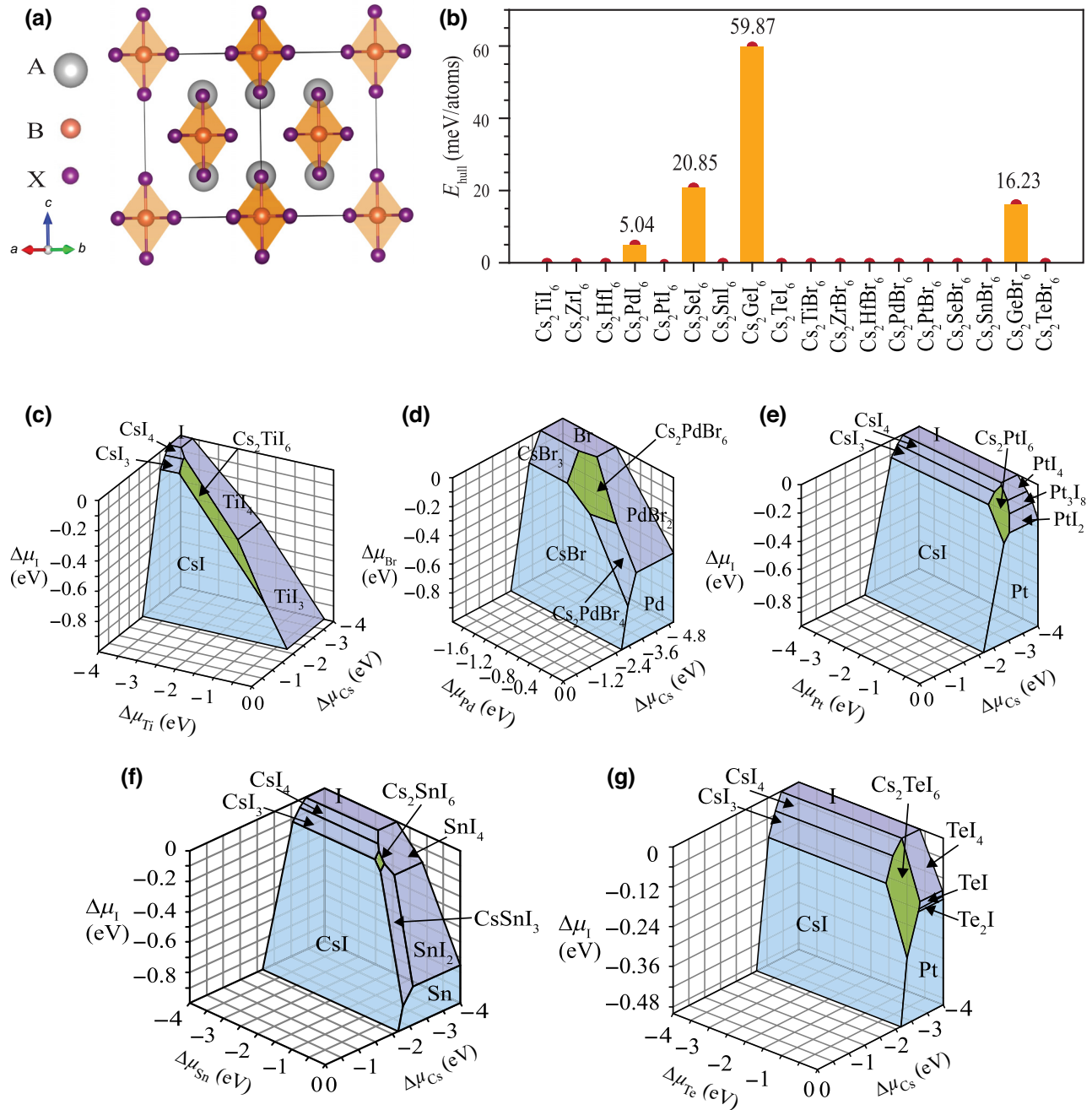
_____

*aftab@iitb.ac.in

024036-1

FIG. 1. (a) Crystal structure of A_2BX_6 compounds in the *Fm-3m* space group. (b) Convex energy hull (E_{hull}) for Cs_2BX_6 (with B = Pd, Pt, Ti, Hf, Zr, Ge, Te, Se, Sn; and X = I, Br). The red semicircle denotes the top of the bar. (c)–(g) Compositional chemical potential phase diagrams of (c) Cs_2TiI_6, (d) Cs_2PdBr_6, (e) Cs_2PtI_6, (f) Cs_2SnI_6, and (g) Cs_2TeI_6 with respect to competing secondary phases. The green area in each diagram shows the stable region of the corresponding material.

optoelectronic applications owing to their better environmental durability, and tunable optical and electronic properties. For example, Cs_2SnI_6 has been studied as a potential candidate in PV [25], LED, PD [3,26], and photocatalyst applications due to its direct-band-gap nature in the visible range (1.1–1.62 eV), high absorption coefficient ($\approx 10^5$ cm^{-1}) [23], and low to high carrier mobility ($\approx$ 2–510 cm^2 V^{-1} s^{-1}) [27–31]. The wide range of measured mobilities of Cs_2SnI_6 can be attributed to variations resulting from different synthesis and characterization methodologies.

Additionally, significant discrepancies have been observed between theoretical and experimental results regarding the transport properties of this material [16,28,32,33]. The

intrinsic limitations to mobility in Cs_2SnI_6 are still not fully understood, and the underlying scattering mechanisms governing carrier transport remain elusive. Therefore, a comprehensive and systematic study encompassing both theoretical and experimental investigations is highly desired to unravel the mobility ambiguity in Cs_2SnI_6 and shed light on its transport characteristics. As of now, this compound exhibits a PCE of only 2.1% [25]. In contrast, substitutional alloying in Cs_2SnCl_6 yields a high photoluminescence quantum yield of 95.4%, making it promising for further exploration in LED applications [34]. Despite considerable investigation into its structural, electronic, and optical properties, the elucidation of charge-carrier dynamics in Cs_2SnI_6 still poses challenges that hinder the optimization of conversion efficiencies.

Similarly, Cs_2TiBr_6, Cs_2TeI_6, and Cs_2PtI_6 are also studied experimentally for PV absorbers, with their band gaps in the ideal visible range, 1.8, 1.5, and 1.4 eV, respectively, along with high absorption coefficients ($\sim 10^5$ cm^{-1}) [35, 36]. Here, device efficiency for Cs_2TiBr_6 as a PV absorber is reported to be 3.3% [37]. An indirect band gap and material instability are reported to be responsible for the poor PCE in this case. In another report, a PV device with Cs_2PtI_6 shows a PCE of 13.88%, which is a remarkable improvement on the reported efficiencies among all the materials belonging to this class to date [36]. The contribution of larger carrier lifetimes along with a direct band gap in the ideal visible range and robust stability help Cs_2PtI_6 to attain the high PCE.

There are reports of synthesizing Pd-based [38] and Zr-based [39] nanomaterials experimentally, but not much has been explored in the direction of optoelectronics. This background clearly indicates that the A_2BX_6 class is extremely interesting and fertile from the application perspective, yet a detailed systematic study on their optoelectronic, carrier transport, and phonon properties connecting these observations is lacking. Moreover, it is also noticed that substitutional alloying and/or doping of pure material is an important strategy to improve optoelectronic properties, which again necessitates an in-depth understanding of the pure materials themselves.

In this paper, we present a detailed and systematic study on the A_2BX_6 class of materials by using highly accurate *ab initio* calculations. First, we have performed a thorough stability analysis, which includes choice of different structural prototypes, thermodynamical stability via chemical potential phase diagram and convex hull analysis, and lattice dynamics simulation. Next, we have studied the electronic properties of the stable compounds using the hybrid Heyd-Scuseria-Ernzerhof (HSE06) functional, which is known to predict reasonably accurate electronic structure information. Optical absorption and PV device parameters are calculated on the promising set of systems showing band gaps in the ideal visible region. Finally, the carrier transport properties of these compounds are studied by considering the important scattering mechanisms. The importance of electron-phonon interactions, calculated within the temperature-dependent Feynman polaron model, is also discussed in some detail. We believe that such an in-depth study not only provides a solid physical basis on this class of semiconductors but will also be immensely beneficial for researchers working on device applications for them in the PV, LED, PD, and photocatalysis fields.

II. COMPUTATIONAL DETAILS

First-principles calculations are carried out using density-functional theory [40] with the projector augmented wave [41] basis set as implemented in the Vienna *Ab Initio* Simulation Package (VASP) [42–46]. A plane-wave energy cutoff of 520 eV, Γ-centered $4 \times 4 \times 4$ k-mesh, and Perdew-Burke-Ernzerhof (PBE) exchange-correlation functional [47] were employed to perform the geometry optimization. The crystal structure was relaxed with force tolerance criteria of 0.001 eV Å^{-1}. The spin-orbit coupling (soc) effect is included while simulating the electronic and optical properties. A hybrid (HSE06) functional [48] is used to calculate the band gap and band edges, which are known to provide a more accurate estimate for the same. Optical absorption spectra are simulated within the independent-particle approximation and then the absorption onset value is scissor-shifted to HSE06 band-gap values. This method makes it possible to accurately assess the SLME for the materials under consideration.

The chemical phase diagrams are drawn using the Chesta software package [49]. Phonon dispersion is calculated using the density-functional perturbation theory using Γ-centered $4 \times 4 \times 4$ k-mesh under the supercell method. The second-order force constant is calculated using $2 \times 2 \times 2$ supercells of primitive cells for cubic structures and in similar proportion for other structures.

Next, the rotational sum rule is applied using the Hiphive package [50] to renormalize the phonon frequencies. Transport calculations are performed using the AMSET code [51], where we have considered three different scattering mechanisms, namely scattering due to acoustic phonons (ADP), ionized impurities (IMP), and polar optical phonons (POP). Piezoelectric scattering is not included due to the centrosymmetric crystal structure of A_2BX_6, whereas screening due to free carriers at high defect concentrations is included. This program uses the Boltzmann transport equation's momentum relaxation-time approximation to determine scattering rates and carrier mobilities.

Polaron-related parameters were simulated via implementing a temperature-dependent Feynman polaron model [52,53]. Born effective charges, and static and high-frequency dielectric tensors were calculated using

density-functional perturbation theory) as implemented in VASP.

The effective mass has been calculated using the following equation:

$$m^* = 3 \left(\frac{1}{m_{xx}^*} + \frac{1}{m_{yy}^*} + \frac{1}{m_{zz}^*} \right) \qquad (1)$$

where m_{ii}^* are the effective masses in the ith directions ($i = x, y, z$) [54–57].

III. STRUCTURAL PROPERTIES AND STABILITY

The vacancy-ordered double perovskites, A_2BX_6, are a class of compounds in which alternate BX_6 octahedra are removed from the ABX_3 unit cell, as shown in Fig. 1(a). In other words, 50% of the B cations are missing compared to the close-packed $A_2BB'X_6$ double-perovskite structure. Here, A, B, and X possess $+1$, $+4$, and -1 oxidation states, respectively. In general, perovskites can crystallize in different structures depending on the ionic radii and electronegativity of the constituent elements. These structures are roughly dictated by a few geometrical parameters, known as Goldschmidt's factors, as defined below:

(a) tolerance factor $t = (r_A + r_X)/(\sqrt{2}(r_B + r_X))$;
(b) octahedral factor $\mu = r_B/r_X$;
(c) radius ratio $r_A/(D_{XX} - r_X)$.

In the above expressions, r_A, r_B, r_X, and D_{XX} are the empirical ionic radii of the constituent elements A, B, and X, and the nearest-neighbor X—X bond length, respectively, in the A_2BX_6 structure. All the calculated parameters are tabulated in Table S1 of the Supplemental Material [58]; see also Refs. [59–65]. The calculated Goldschmidt's tolerance factor predicts the formation of cubic structures [24,28,29,36,38,66]. Though these geometrical factors represent an important guideline to assess the formation of plausible structures for a given perovskite, they are not sufficient conditions [67].

In this work, we have investigated the following A_2BX_6 compounds: A = Cs; B = Ge, Te, Se, Sn, Pd, Pt, Ti, Zr, Hf; and X = I, Br. For each compound, we have considered the seven most common structural prototypes, as reported in the International Crystal Structure Database (ICSD) [68,69], for the A_2BX_6 class of compounds. The space groups of these seven structures are Fm-$3m$ (cubic), $I4/m$ (tetragonal), $I4/mmm$ (tetragonal), P-$3m1$ (hexagonal), $Pnma$ (orthorhombic), $P4/mnc$ (monoclinic), and $P12_1/c1$ (monoclinic). These crystal structures are shown in Fig. S1 of the Supplemental Material [58]. Most of these structures are very similar in symmetry and differ in

energy within only a few milli-electron volts (3–4 meV). After structural optimization, the lowest-energy structure for most of the above set of compounds turns out to be cubic (Fm-$3m$). It has been observed experimentally that several Cs-based iodide and bromide compounds indeed crystallize in the cubic space group [24,28,29,36,38,66].

To further assess the chemical stability, we have calculated the convex hull energies (E_{hull}) of these compounds with respect to possible secondary phases available in the ICSD, the Open Quantum Materials Database [70,71], and the Materials Project Database [72]. As evident from Fig. 1(b), most of the compounds lie on the convex hull, i.e., $E_{\text{hull}} = 0$, except for Cs_2GeI_6, Cs_2SeI_6, Cs_2PdI_6, and Cs_2GeBr_6, confirming the stability of the former. For the remaining four compounds, E_{hull} ranges between 5 and 60 meV/atom, indicating the likelihood of chemical metastability or instability.

Next, in order to explore the most probable secondary phases during synthesis of Cs_2BX_6 materials, we have calculated the compositional phase diagrams (chemical potential) for materials on the convex hull. More details about the phase-diagram calculations and analysis are given in Sec. A of the Supplemental Material [58]. Figures 1(c)–1(g) show the phase diagrams for those materials which show potential for optoelectronic applications (based on their band gap, and optical and transport properties, as discussed later). The phase diagrams for the remaining compounds are displayed in Fig. S2 of the Supplemental Material [58]. The green-shaded portion shows the stability region for each of these materials. The extent of the stability region directly correlates with the ease or difficulty of experimental synthesis. The theoretically optimized lattice parameters and bond lengths (B—X) of all the stable compounds in their cubic structure are displayed in Table S2 of the Supplemental Material [58].

Further, we have checked the dynamical stability of these compounds by calculating phonon dispersions, as shown in Fig. S3 of the Supplemental Material [58]. The absence of any visible imaginary phonon modes indicates dynamical stability of these compounds. For Cs_2SnI_6 and Cs_2TiI_6, one can observe small negative phonon frequencies, the magnitude of which decreases with increasing supercell size [73]. This is because the latter capture the effect of higher-order interatomic force constants more accurately. Additionally, in line with recent findings [74,75], the presence of these small imaginary frequencies in Cs_2SnI_6 can be attributed to a subtle rotation of the octahedral structure, further supporting our previous observations. Nevertheless, these compounds are already experimentally synthesized, and hence naturally stable [28,76].

Following stability analysis, we have further studied the electronic structures of 15 (14 stable and one metastable) compounds in the next section.

IV. ELECTRONIC STRUCTURE

Band-structure calculations for all the compounds are initially performed using the Perdew-Burke-Ernzerhof (PBE) exchange-correlation functional [47]. As the PBE functional is well known to underestimate the band gap, we also employ the hybrid Heyd-Scuseria-Ernzerhof (HSE06) [48] functional, which gives a more accurate estimate of band gaps in comparison to experiment. The spin-orbit coupling (soc) effect in included in all the calculations. Band structures for four potential compounds calculated using the PBE + soc functional (band gaps are scissor-shifted to HSE06 + soc values) are shown in Fig. 2. In the A_2BX_6 class of compounds, the topology of band structure

calculated using the HSE06 + soc functional is very similar to that calculated using the PBE + soc functional except for the enlargement of the band gap in the former (see Fig. S4 of the Supplemental Material [58] for a few representative cases).

Figure 2 also shows the optical transition probability (p^2), and total or orbital projected density of states (PDOS) of Cs_2TiI_6, Cs_2PdBr_6, Cs_2PtI_6, Cs_2SnI_6, and Cs_2TeI_6. The square of the dipole transition matrix element is defined as $p^2 = |\langle n|\hat{p}|m\rangle|^2$, where n and m are the two quantum states for which the transition probability is calculated, and $\hat{p}$ is the dipole operator [77]. The HSE06 + soc band-gap values for the respective compounds are provided
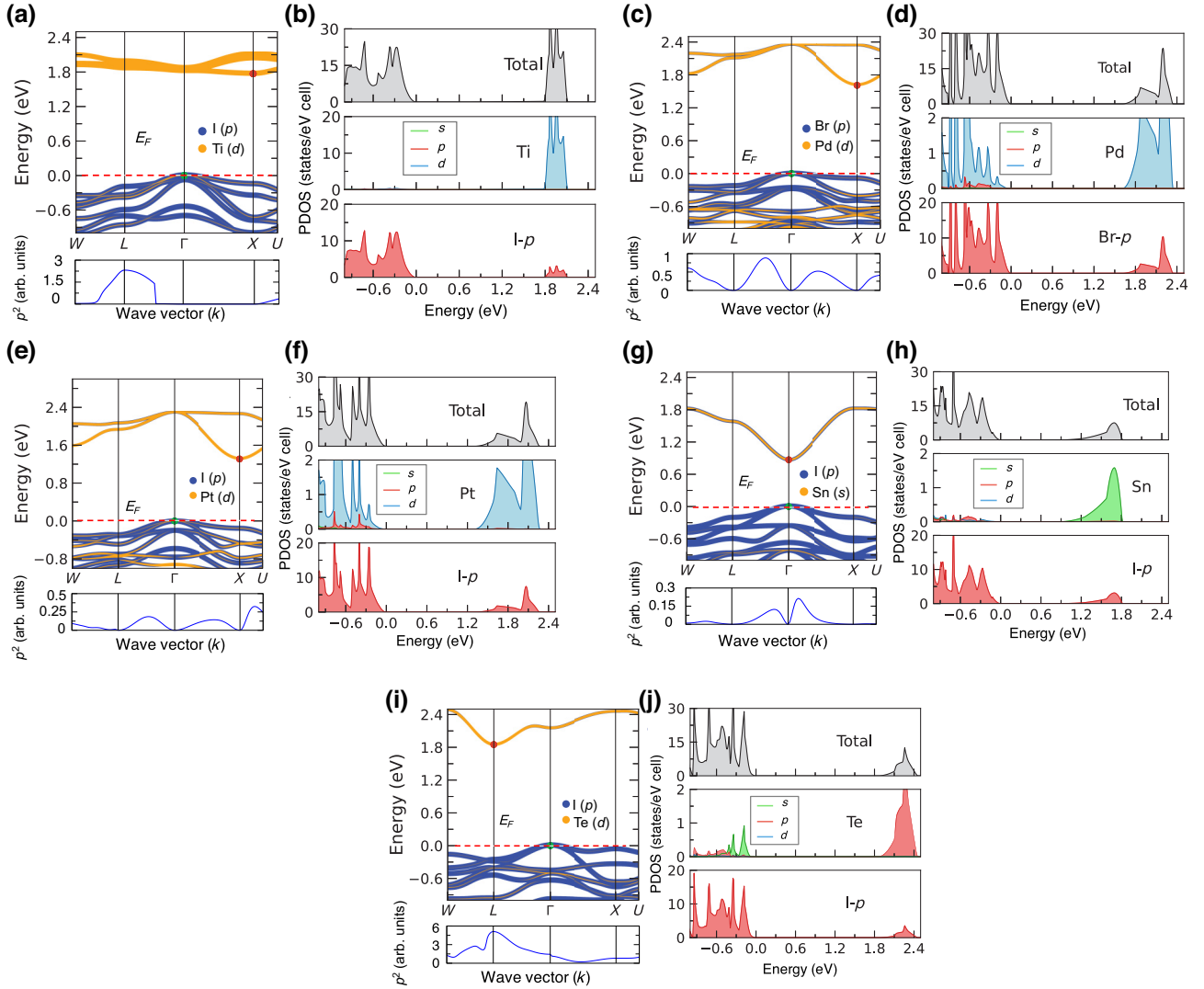

FIG. 2.   (a),(c),(e),(g),(i) Band structure and the square of the dipole transition matrix elements (p^2) for (a) Cs_2TiI_6, (c) Cs_2PdBr_6, (e) Cs_2PtI_6, (g) Cs_2SnI_6, and (i) Cs_2TeI_6. (b),(d),(f),(h),(j) Projected density of states (PDOS) for the same set of compounds, respectively. All the calculations are done using the PBE functional, including the spin-orbit coupling (soc) effect, while the band gap is scissor-shifted to HSE06 + soc calculated values. In the band-structure plots, valence-band maxima (VBM) and conduction-band minima (CBM) are indicated via green and red circles, respectively. The PDOSs are shown only for those atoms and/or orbitals that have visible contributions, the rest are negligibly small.

in Table I. The band structures, PDOSs, and respective band-gap values for other compounds are provided in Figs. S5–S7 and Tables S3 and S4 of the Supplemental Material [58]. In the *Fm-3m* phase, the estimated band-gap values lie within 0.72 to 4.31 eV for different compounds. Optical transitions at the fundamental direct gaps are dipole-forbidden for all the compounds, as confirmed by the calculated optical transition probability (p^2). Here the presence of inversion symmetry plays the key role to induce parity-forbidden transitions for these compounds, effectively increasing the optical band gap.

In the present study, we considered nine different elements at the B site, belonging to four distinct groups in the periodic table. Despite all elements having +4 oxidation state, their valence electron orbital configurations differ, resulting in distinct electronic structures, including variations in band structure and band-gap types among the compounds. In the following, we shall discuss the electronic structure of representative compounds from each group and compare them with the electronic structures of other compounds within the same group, including different halides.

For Cs_2TiI_6, the band gap is indirect in nature, with conduction band minimum at X and valence band maximum at Γ. But the direct band gap at Γ is very close to the indirect band-gap value (~ 50 meV) (Table I). From the orbital projected density of states, we observe that the CBM comprises Ti d and I p, i.e., B d and X p [see Figs. 2(a) and 2(b)]. The electronic band-gap value is 1.77 eV, which is overestimated by 0.75 eV with respect to the experimental value (1.02 eV) [24]. The calculated optical band gap lies within 100 meV of the fundamental direct gap. Apart from that, the large difference between the calculated electronic band gap and the optically measured experimental band gap can be attributed to the excitonic effect (not taken into account here) and the defects present in the measured sample, as discussed by Cucco *et al.* [78]. All the electronic structure information for the rest of the

compounds can be found in Figs. S5–S7 and Tables S3 and S4 of the Supplemental Material [58]. It is clearly evident that the band gap increases from Ti $\rightarrow$ Zr $\rightarrow$ Hf and also with I $\rightarrow$ Br. In this group, only Cs_2TiI_6 shows a band gap in the ideal visible region.

Cs_2PdI_6 shows an indirect band gap in both the space groups with CBM at X and VBM at Γ (see Fig. S5 of the Supplemental Material [58]). The optically allowed direct band gap (0.88 eV) is very close to the indirect band-gap values (0.72 eV) (shown in Table I). Experimentally, Cs_2PdI_6 nanocrystals [66] are synthesized and a band gap of 0.69 eV is reported. The reason behind the overestimation might be similar to what is explained for the case of Cs_2TiI_6. In this case, the CBM comprises Pd d and I p orbitals, while the VBM is composed of only the I p orbital (see Fig. S5 of the Supplemental Material [58]). Like Cs_2PdI_6, Cs_2PtI_6, Cs_2PtBr_6, and Cs_2PdBr_6 show similar orbital contributions at both the CBM and VBM, giving rise to the indirect nature of the band gap. Their band-gap values along with the formation energetics and differences between the direct and indirect band gaps are presented in Tables S3 and S4 and Fig. S5 of the Supplemental Material [58] and in Figs. 2(c) and 2(e). For Cs_2PtI_6 and Cs_2PdBr_6, the calculated band gaps are close to experimentally reported values for Cs_2PtI_6 powder [79,80] and Cs_2PdBr_6 nanocrystals [38,66], respectively. Here, we observe an increase in band gap on going from Pd $\rightarrow$ Pt and also from I $\rightarrow$ Br. In this case, Cs_2PdI_6, Cs_2PtI_6, and Cs_2PdBr_6 compounds show band gaps within the ideal visible range.

The band-structure analysis of Cs_2TeI_6 reveals that it has an indirect band gap with a value of 1.85 eV, consistent with the study by Maughan *et al.* [28]. From PDOS analysis, we observe that the CBM comprises Te p and I p orbitals, whereas the VBM is made up of the I p orbital [see Figs. 2(i) and 2(j)]. The calculated electronic band-gap value of 1.85 eV is 0.26 eV higher than the experimentally reported value [28]. For Cs_2TeBr_6, the band-gap nature and orbital contribution at both the CBM and VBM are similar

TABLE I. Simulated band gap (E_g), difference between electronic and optically allowed direct band gaps (ΔE_g^{da}), short-circuit current density (J_{SC}), open-circuit voltage (V_{OC}), current density (J_{max}) and voltage (V_{max}) at maximum power, fill factor (FF), and spectroscopic limited maximum efficiency (SLME) for Cs_2TiI_6, Cs_2PdBr_6 Cs_2PtI_6 Cs_2SnI_6, Cs_2TeI_6, and Cs_2PdI_6 compounds. In the third column, (ID) and (D) indicate indirect and direct nature of band gaps, respectively. All the device-related parameters are shown for 500-nm thickness at 298 K. Experimental band gaps (E_g^{expt}) and reference sources are also listed for comparison.

Compound	E_g^{expt} (eV)	E_g(HSE06 + soc) (eV)	ΔE_g^{da} (meV)	J_{SC} (mA cm^{-2})	J_{max} (mA cm^{-2})	V_{OC} (V)	V_{max} (V)	FF	SLME η (%)
Cs_2TiI_6	1.02 [24]	1.77 (ID)	72	16.64	16.34	1.50	1.39	0.91	22.78
Cs_2PdBr_6	1.6 [38], 1.69 [66]	1.61 (ID)	110	17.62	17.26	1.35	1.25	0.91	21.63
Cs_2PtI_6	1.25 [79], 1.37 [80], 1.4 [36]	1.31 (ID)	149	22.23	21.66	1.08	0.98	0.89	21.26
Cs_2SnI_6	1.25 [28], 1.62 [29]	0.87 (D)	41	32.58	31.33	0.72	0.64	0.85	20.07
Cs_2TeI_6	1.59 [28]	1.85 (ID)	190	12.95	12.72	1.55	1.45	0.92	18.44
Cs_2PdI_6	1.41 [66]	0.72 (ID)	166	43.20	40.94	0.54	0.46	0.81	18.97

TABLE II.   Calculated electron effective mass m_e^* (in units of electron rest mass m_0), high-frequency and static dielectric constants ϵ_∞ and ϵ_{static}, effective phonon frequency ν_{eff}, Fröhlich coupling constant for electrons α_e, electron mobility μ_e, and polaron radius $l_p(e)$ for Cs_2TiI_6, Cs_2PdBr_6, Cs_2PtI_6, Cs_2SnI_6, Cs_2TeI_6, and Cs_2PdI_6 compounds. The corresponding set of parameters for holes are displayed in Table S5 of the Supplemental Material [58].

Parameters	Cs_2TiI_6	Cs_2PdBr_6	Cs_2PtI_6	Cs_2SnI_6	Cs_2TeI_6	Cs_2PdI_6
m_e^* (m_0)	1.66	0.66	0.49	0.31	0.35	0.61
ϵ_∞	4.91	4.15	4.82	5.04	4.89	7.58
ϵ_{static}	10.81	7.21	8.40	10.41	11.21	11.68
ν_{eff} (THz)	3.77	3.16	2.16	2.60	2.71	2.25
α_e	4.23	2.66	2.44	2.02	2.38	1.38
μ_e (cm^2 V^{-1} s^{-1})	1.5	11.9	22.7	31.4	27	51.3
$l_p(e)$ (Å)	29.40	32.75	25.88	32.48	30.92	35.33

to those of Cs_2TeI_6. The related electronic properties can be found in Table S4 and Fig. S6 of the Supplemental Material [58]. All the electronic structure information for Cs_2SeBr_6 can be found in Table S4 and Figs. S6(c) and S6(d) of the Supplemental Material [58], and shows similar orbital characteristics.

For Cs_2SnI_6, the calculated electronic band-gap value (E_g) is 0.87 eV, which is direct in nature and matches reasonably well with the computed value (0.88 eV) reported earlier [28]. There are several experimental reports on Cs_2SnI_6, and the measured band gap lies in the range 1.25–1.6 eV [27,29,81]. From orbital analysis, we observe that the CBM is made up of Sn s and I p orbitals, and the VBM comprises the I p orbital [see Figs. 2(g) and 2(h)]. For Cs_2SnBr_6, the band-gap nature and orbital contribution at both the CBM and VBM remain similar to those of Cs_2SnI_6. The related electronic properties can be found in Table S4 and Figs. S6(a) and S6(b) of the Supplemental Material [58].

To summarize the electronic properties, one should note that, for indirect-band-gap compounds, the calculated electronic band gaps are overestimated as compared to the experimentally reported optical band gaps in several cases [78]. Contrary to previous reports, the optical band gaps are close to the lowest direct band gaps, confirmed by our calculation of the optical transition probability. We believe that the most probable reasons for the overestimation of theoretical E_g can be attributed to the excitonic effects (not included in the present calculations) and defects present in the experimental samples, as discussed by Cucco *et al.* [78]. It has been observed previously that, due to low carrier effective mass and higher dielectric constants, iodides show much lower (almost an order of magnitude) excitonic binding energy (E_b) as compared to their Cl counterparts. For example, E_b for Cs_2TiI_6 is 0.22 eV whereas for Cs_2TiCl_6, $E_b = 1.73$ eV. Cs_2SnI_6 has even lower E_b of 130 meV [82].

In our present study, most of the compounds proposed for PV applications are iodides (Cs_2TeI_6, Cs_2SnI_6, Cs_2TiI_6, Cs_2PtI_6, Cs_2PdI_6, and Cs_2PdBr_6) and hence we believe

the influence of excitonic effects and the corresponding impact on the potentiality for PV performance will be relatively much smaller. Nevertheless, such E_b values are not appreciably small, and hence require further device engineering in order to make them better for PV application. From the materials perspective, alloying can be done to reduce E_b [83]. From the device perspective, there are a few mechanisms that are being used for exciton dissociation in newer-generation PV devices for excitonic solar cells, e.g., field-assisted dissociation, interfacial engineering, incorporating specific tunnelling layers, etc. [84–86].

From the electronic structure analysis, we notice that the band gaps of Cs_2TeI_6, Cs_2SnI_6, Cs_2PdI_6 (*Pnma*), Cs_2PtI_6, Cs_2TiI_6, and Cs_2PdBr_6 lie in the ideal visible range for photovoltaic application. Therefore, we shall now focus on the optical properties of these six compounds along with the well-known descriptor "spectroscopic limited maximum efficiency" (as proposed by Yu *et al.* [87]) to better understand their potential as solar absorber.

V. OPTICAL PROPERTIES

The optical absorption ($\alpha(\omega)$) mainly depends on two factors: (1) the optical joint density of states (JDOS) and (2) the optical transition strength (p^2). In general, $\alpha(\omega)$ can be defined as [88]

$$\alpha(\omega) = \frac{2\pi}{\hbar} \int |\langle n| \hat{H} |m\rangle|^2$$
$$\times \frac{2}{8\pi^3} \delta(E_m(\vec{k}) - E_n(\vec{k}) - \hbar\omega)\, d^3k, \quad (2)$$

where $\hbar\omega$ is the photon energy, the integration spans over the entire Brillouin zone, and $|\langle n| \hat{H} |m\rangle|$ is the transition matrix element between the bands n and m. Within the approximation that the quantity $\langle n| \hat{H} |m\rangle$ varies extremely slowly with $\vec{k}$ or even is independent of $\vec{k}$, the optical
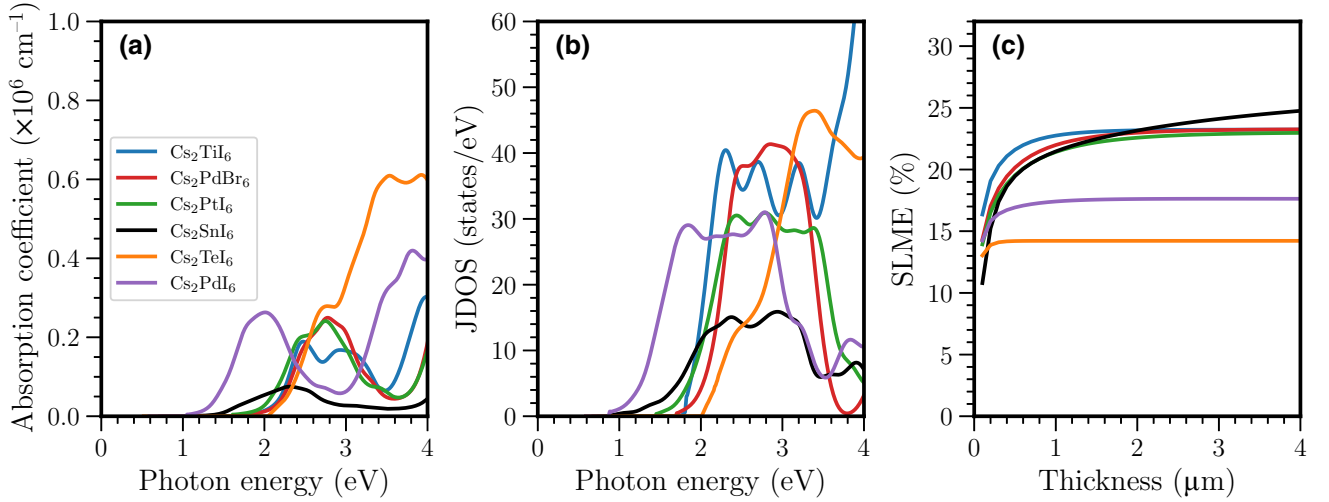
FIG. 3. (a) Absorption coefficient versus incident photon energy, (b) the joint density of states versus incident photon energy, and (c) spectroscopic limited maximum efficiency (at 298 K) versus film thickness for Cs_2TiI_6, Cs_2PdBr_6, Cs_2PtI_6, Cs_2SnI_6, Cs_2TeI_6, and Cs_2PdI_6 compounds.

absorption can be rewritten as

$$\alpha(\omega) = \frac{2\pi}{\hbar} |\langle n| \hat{H} |m\rangle|^2$$

$$\times \int \frac{2}{8\pi^3} \delta(E_m(\vec{k}) - E_n(\vec{k}) - \hbar\omega) \, d^3k. \quad (3)$$

Here, $\int (2/(8\pi^3)) \delta(E_m(\vec{k}) - E_n(\vec{k}) - \hbar\omega) \, d^3k$ is nothing but the JDOS. In other words, the optical absorption is directly proportional to the square of the dipole transition matrix element and JDOS.

Figure 3(a) shows the absorption coefficients for the six above-mentioned promising compounds Cs_2TiI_6, Cs_2PdBr_6, Cs_2PtI_6, Cs_2SnI_6, Cs_2TeI_6, and Cs_2PdI_6. All these compounds can act as potential solar absorbers, as their absorption coefficients are as high as 10^5–10^6 cm^{-1} in the visible range. This is because of the high joint density of states near E_g^{da}, as seen in the simulated JDOS plot in Fig. 3(b). In a few cases, the optical absorption is high despite the JDOS being relatively small. In such scenarios, the role of the square of the dipole matrix elements (p^2), as indicated in Eq. (3), becomes crucial for the overall magnitude of $\alpha(\omega)$.

The absorption coefficient can also be directly connected to the frequency-dependent dielectric function of a semiconductor via the equation

$$\alpha(E) = \frac{2\omega}{c} \sqrt{\frac{\sqrt{\epsilon_{re}^2 + \epsilon_{im}^2} - \epsilon_{re}}{2}}, \quad (4)$$

where E is the incident photon energy, ω is the angular frequency (related to E via $E = \hbar\omega$), c is the velocity of light, and ϵ_{re} and ϵ_{im} are the real and imaginary parts of

the dielectric function, respectively. To assess the theoretical PV efficiency, we have used the well-known metric, the spectroscopic limited maximum efficiency. In an earlier study by Kirchartz et al. [89], it has been shown that, in the high-mobility limit, for excitonic and bulk heterojunction solar cells, the principle of detailed balance ensures the applicability of the Shockley-Queisser (SQ) formalism. SLME is a modified and improved version of the SQ formalism in which a material's absorption coefficient is considered to calculate the absorptivity instead of the step-like function originally used. As such, the estimate of SLME can give a relative idea about the potential of one material over another, if not an accurate estimate of PV efficiency. The said formalism has been previously used even for materials with high exciton binding energies [90,91].

Figure 3(c) shows the thin-film thickness dependence of SLME, which turns out to be > 15% for all six compounds. Interestingly, we can see higher SLME for Cs_2PdI_6, Cs_2PtI_6, and Cs_2TiI_6 compounds as compared to Cs_2SnI_6. Such increased SLME is essentially attributed to increased high absorption spectra due to I p to Pd d, Pt d, or Ti d orbital transition as well as suitable band gaps. In Table I, we present the simulated device parameter values for the six compounds: short-circuit photocurrent density (J_{SC}), open-circuit voltage (V_{OC}), fill factor (FF), maximum current density (J_{max}), and maximum voltage (V_{max}) obtained from the SLME calculation. The detailed description and method of calculation of these parameters can be found in Sec. C of the Supplemental Material [58].

As expected, materials with higher band gaps exhibit higher V_{OC} values, while materials with lower band gaps have higher J_{SC} values. The other compounds do not have SLME values as high as these six materials owing to higher

band gaps. Their absorption coefficients and SLME values are shown in Figs. S8 and S9, respectively, of the Supplemental Material [58]. Furthermore, it is worth noting that the band gaps of other compounds are distributed within the visible range (larger than 1.8 eV), which makes them suitable for LED and photocatalytic water splitting applications. Alloying at B and X sites are other avenues to tune the optoelectronic properties of these systems and hence make them suitable for different applications.

VI. TRANSPORT PROPERTIES

Detailed analysis of the optoelectronic properties and calculation of solar efficiency (SLME) reveals six compounds to be promising. This can be attributed to their optimal band gaps falling within the ideal visible region of the solar spectrum coupled with their excellent absorption coefficients. However, in a practical photovoltaic device, extraction of charge carriers is one of the key components determining the power conversion efficiency. As such, the mobility of the charge carriers is an integral quantity dictating the promise of a semiconductor for solar harvesting. Most of the past theoretical studies on photovoltaic materials rely on calculation of transport properties based on the constant-relaxation-time approximation. Within this approximation, all the scattering mechanisms are averaged out via a single relaxation time (chosen to be approximately 10 fs). This practice, however, can be misleading, as the carrier relaxation time is a complex parameter which depends sensitively on a number of physical properties and can be significantly different for different materials belonging to the same class (as illustrated in this study).

In this section, we perform a thorough analysis of the carrier mobilities of these compounds, considering three relevant scattering mechanisms, namely, scattering due to acoustic phonons (ADP), ionized impurities (IMP), and polar optical phonons (POP). We have excluded piezoelectric scattering due to the inherent centrosymmetry present in these compounds. A detailed formalism for these scattering mechanisms is shown in Sec. D of the Supplemental Material [58]. In Figs. 4 and 5, we show the temperature and defect-concentration dependences of electron and hole mobilities (μ_e and μ_h) for six promising compounds. The contributions of individual scattering mechanisms to these mobilities for the six compounds are shown in Figs. S10 to S15 of the Supplemental Material [58].

Figure S16 of the Supplemental Material [58] displays the total relaxation times of the six compounds at varying defect concentrations, ranging from 10^{10} to 10^{20} cm^{-3} at three different representative temperatures (100 K, 300 K, and 500 K) for both hole and electron transport. For defect concentrations in the low to moderate range, the relaxation time remains almost constant. However, as the defect

concentration increases, relaxation times vary in an irregular manner. To comprehend the cause of this anomalous behavior, a more in-depth analysis was conducted. The relaxation times for all three scattering mechanisms were calculated for each compound, and are plotted in Figs. S17 to S22 of the Supplemental Material [58]. A close inspection of these data confirms that, in the low to moderate concentration range, the primary scattering mechanism is due to POP scattering. In contrast, as the concentration increases into the higher range, the dominant scattering mechanism shifts to IMP scattering, resulting in the emergence of anomalous behavior. Such unusual behavior is also reflected in the mobility shown in Fig. 4.

Regarding the behavior of the mobilities of the individual compounds, one can notice that, at low temperature (100 K), the hole mobility (μ_h) is highest for Cs$_2$TiI$_6$ ($\sim$ 20.9 cm^2 V^{-1} s^{-1}). With increasing temperature, μ_h decreases slowly to reach a shallow minimum and increases again with increasing defect concentration. At higher temperature, Cs$_2$PdI$_6$ shows the highest hole mobility ($\sim$ 5.9 cm^2 V^{-1} s^{-1} at 300 K, and $\sim$ 4.2 cm^2 V^{-1} s^{-1} at 500 K) among all the compounds. This compound also shows the highest electron mobility ($\sim$ 183 cm^2 V^{-1} s^{-1} at 100 K, $\sim$ 51 cm^2 V^{-1} s^{-1} at 300 K, and $\sim$ 32 cm^2 V^{-1} s^{-1} at 500 K) throughout the temperature range. At room temperature, the hole mobilities remain relatively low but, except for Cs$_2$TiI$_6$, the electron mobilities show moderate to high values ($\sim$ 13–63 cm^2 V^{-1} s^{-1}). This is commensurate with the electronic band structures of these compounds, where the VBM shows flat bands whereas the CBM is more dispersive. Consequently, *n*-type doping could prove advantageous for efficient charge-carrier collection in photovoltaic devices, aligning with the experimental findings for this class of compounds [27,29,92].

A closer look at the individual contributions from the different scattering mechanisms shows that, at low to moderate defect concentrations ($< 10^{18}$ cm^{-3}), POP scattering is the dominant scattering mechanism limiting the mobilities. With increasing temperature, the number of activated polar optical phonons increases, and as a result we see a decrease in overall mobility on going from 100 K $\to$ 300 K $\to$ 500 K. At higher defect concentrations (10^{18}–10^{20} cm^{-3}), we see that IMP scattering begins to dominate, as can be seen from Figs. S10(a)–S10(c) to S15(a)–S15(c) of the Supplemental Material [58]. At these concentrations, there is one more mechanism that starts to impact the carrier mobility, which is the screening of polar optical phonons by free carriers. This, in effect, reduces the POP scattering, effectively increasing the overall mobility in some cases. Now, the temperature also has an effect on this screening mechanism. At higher temperatures, there are more activate polar optical phonons, which require a higher density of free carriers to effectively screen the Coulomb field created by these phonons. This is clearly evident from Figs. S10(a)–S10(c) to S15(a)–S15(c) of the
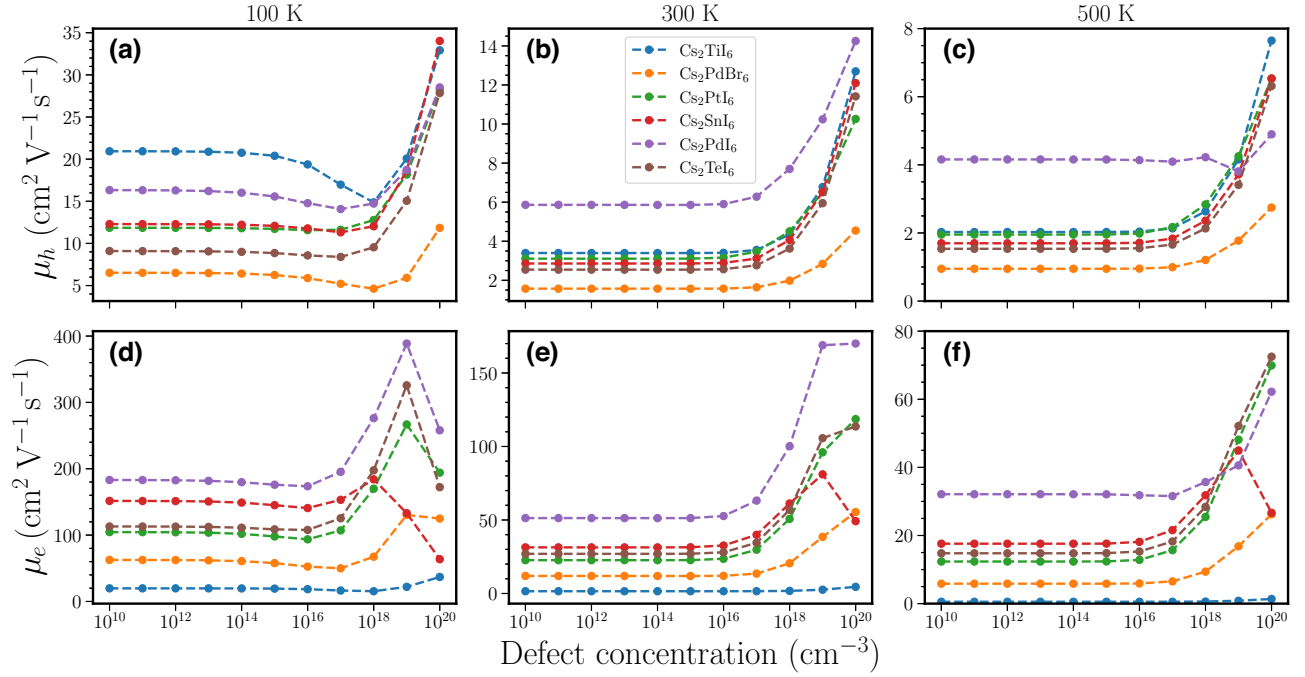
FIG. 4. (a)–(c) Hole mobility (μ_h) and (d)–(f) electron mobility (μ_e) for Cs$_2$TiI$_6$, Cs$_2$PdBr$_6$, Cs$_2$PtI$_6$, Cs$_2$SnI$_6$, Cs$_2$PdI$_6$, and Cs$_2$TeI$_6$ compounds as a function of defect concentration at three different temperatures, $T = 100$ K, $T = 300$ K, and $T = 500$ K, as shown.

Supplemental Material [58]. In all the cases, ADP scattering remains low, which is common in hybrid perovskites arising out of small deformation potentials [51,93].

In Figs. 5(a)–5(f), we show average hole and electron mobilities at temperatures ranging from 100 K to 500 K for three different defect concentrations, low (10^{10} cm^{-3}), moderate (10^{15} cm^{-3}), and high (10^{20} cm^{-3}). Because of the weak dependence on IMP scattering at low to moderate defect concentrations, we see that the carrier mobility remains similar in these two defect concentrations. But we can see that, at higher concentrations, IMP starts to dominate. As such, controlling the defect concentrations can impact device efficiencies, not only because, at higher defect concentrations, IMP becomes the dominant scattering mechanism, but also because the prevalence of free carriers will start to screen the POP scattering effect. As expected, the overall mobility has a strong temperature dependence for most of the compounds and remains high to moderate for the electrons, whereas the hole mobility values remain consistently low.

The above analysis reveals that in the A$_2$BX$_6$ class, polar optical phonons play a dominant role at the realistic defect concentrations relevant for photovoltaic applications. As such, next we study the properties of the polaronic states via calculating the Fröhlich interactions under the temperature-dependent Feynman polaron model [94]. In polar semiconductors, for example, halide perovskite and its derivatives, the interaction between charge carriers and the macroscopic electric field generated by

longitudinal optical (LO) phonons is well known to be the dominant scattering mechanism near room temperature, which is expected to be the case for our studied materials as well [32,51,53,92,95–97].

To investigate the same, we studied the influence of changing B site in A$_2$BX$_6$ on the electron-phonon coupling. Within the Fröhlich interaction model, the interaction strength (α) is defined as

$$\alpha = \frac{1}{4\pi\epsilon_0} \frac{1}{2} \left(\frac{1}{\epsilon_\infty} - \frac{1}{\epsilon_{\text{static}}} \right) \frac{e^2}{\hbar\omega_{\text{LO}}} \left(\frac{2m^*\omega_{\text{LO}}}{\hbar} \right)^{1/2}, \quad (5)$$

where ϵ_0 is the vacuum dielectric constant, ϵ_∞ and ϵ_{static} are the high-frequency and static dielectric constants of the semiconductor, $\hbar$ is the reduced Planck constant, ω_{LO} is the characteristic angular LO frequency where all the infrared-active optical phonon branches are taken into account via a spectral average [53], and m^* is the carrier effective mass. Table II displays all the associated values related to Fröhlich interaction for electrons for the six compounds. The corresponding list of parameters for the holes for these six compounds are reported in Table S5 of the Supplemental Material [58].

To validate our simulation, we compare the calculated values of α for Cs$_2$SnI$_6$ with recent literature and observe a fair agreement [32]. In the case of the A$_2$BX$_6$ class, calculated α values lie in the moderate range ($1 < \alpha < 6$). Estimated values of the polaron radius (l_p) indicate the formation of large polarons, similar to what is observed
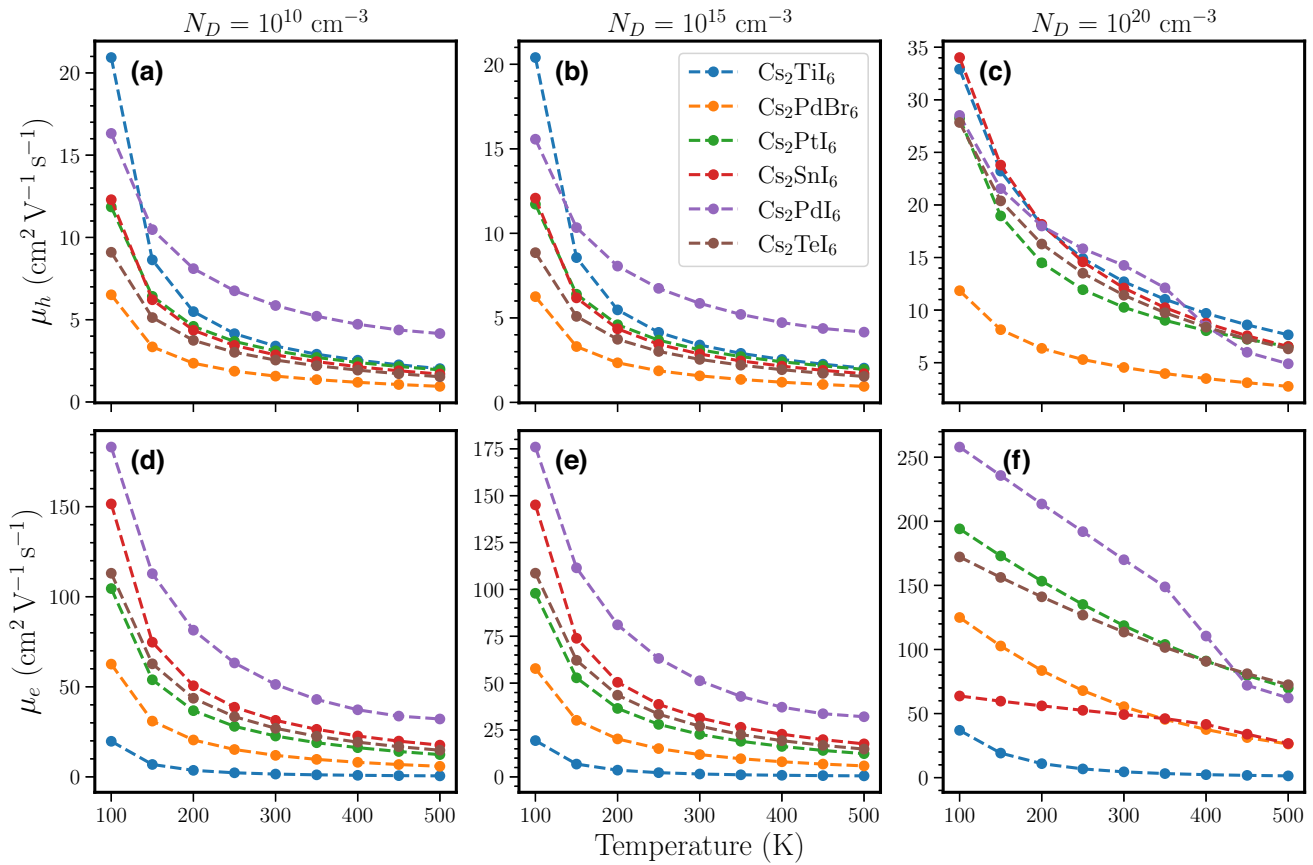
FIG. 5. (a)–(c) Hole mobility (μ_h) and (d)–(f) electron mobility (μ_e) for Cs_2TiI_6, Cs_2PdBr_6, Cs_2PtI_6, Cs_2SnI_6, Cs_2PdI_6, and Cs_2TeI_6 compounds as a function of temperature at three different defect concentrations, $N_D = 10^{10}$ cm^{-3}, 10^{15} cm^{-3}, and 10^{20} cm^{-3}, as shown.

for hybrid halide perovskites and double perovskites [53, 97,98]. The α_e value is highest for Cs_2TiI_6 mainly due to higher electron effective mass compared to the other compounds. Additionally, taking an inference from the electronic structure of these materials, we see that CBM in Cs_2TiI_6 has a contribution from Ti d and I p orbitals whereas for Cs_2SnI_6, it is Sn s and I p orbitals. Now, Ti d orbitals are more localized arising out of the flat band and hence higher effective mass. For other compounds, we see more dispersive bands (see Fig. 2) at the CBM, and the corresponding α values are in the range close to that of Cs_2SnI_6. Interestingly, the hole mobility turns out to be significantly lower than the electron mobility.

To conclude, large polarons are the main carrier related to the moderate mobility for our studied compounds. These crucial observations clearly indicate the importance of studying charge-carrier behavior in the A_2BX_6 class of compounds and its implications in future applications. While our study provides valuable insights into the transport properties, it is important to acknowledge the potential influence of strongly bound excitons on charge carriers. These excitons can act as scattering centers, introducing obstacles and influencing mobility. Elevated

temperatures may increase exciton dissociation, further affecting charge-carrier mobility. In the case of strong exciton binding ($E_b \gg E_F$) falling within the strong-coupling regime beyond the Fröhlich model [99], exploring this aspect requires specialized investigation beyond the scope of the present study.

Most of our proposed compounds have an indirect band gap and the question of their applicability as potential PV absorbers is obvious. Recently, one of the authors, Kangsabanik *et al.* [57], reported that semiconductors with indirect band gaps can also be relevant for photovoltaics given that their band gaps fall in the ideal visible region and the optically allowed direct gap is not far away from the indirect one. When a material possesses an indirect band gap, there are several factors that one should look at to determine its suitability as a photovoltaic absorber. These factors involve (1) the value of the optically allowed direct band gap, (2) the order of magnitude of absorption coefficients, (3) the carrier lifetime, and (4) defect properties. In our present study, the optically allowed direct band gaps for the proposed potential materials indeed lie within the ideal visible range. In addition, these optically allowed direct band gaps are not too far from the electronic

indirect band gap. Further, we studied the transport properties within the variable-relaxation-time framework, which captures the effect of various scattering mechanisms in the formalism and yields a reliable estimate of carrier lifetime. Such an estimate gives an idea about the defect concentrations and charge-carrier collection by the electrodes. All these factors indicate the potentiality of our selected compounds for PV applications. A more in-depth study of the defect formation energies for various intrinsic defects is our future endeavour.

VII. CONCLUSION

In summary, we performed an accurate and systematic investigation of Pb-free vacancy-ordered double perovskites (A_2BX_6) from the optoelectronic application perspective. We carried out a thorough stability analysis considering different structural prototypes and carefully simulating the convex hull energy diagram including all possible secondary phases. We found 14 compounds to be stable and one in the metastable phase. For the stable compounds, we further simulated the compositional phase diagrams to assist experimentalists in identifying the most probable secondary phases that might emerge during synthesis.

Next, a careful electronic structure analysis reveals that six compounds, namely Cs_2TeI_6, Cs_2SnI_6, Cs_2PdI_6, Cs_2PtI_6, Cs_2TiI_6, and Cs_2PdBr_6, possess optically allowed band gaps in the ideal visible range (0.8–1.85 eV). Detailed investigation of the optical properties confirms that a few of these compounds possess favorable optoelectronic properties facilitating better efficiency than some of the existing ones.

A close inspection of transport properties reveals that Cs_2PdBr_6, Cs_2PtI_6, Cs_2SnI_6, Cs_2PdI_6, and Cs_2TeI_6 compounds acquire moderate to high electron mobilities ($\sim$ 13–63 cm^2 V^{-1} s^{-1}). In all the cases, polar optical phonons (POP) remain the dominant scattering mechanism at low to moderate defect concentrations. At high defect concentrations, ionized impurity scattering starts to dominate while the accumulation of free carriers shows a screening effect on the POP scattering.

This study is expected to facilitate the necessary basis and guidance for future experimental synthesis of some of these compounds to achieve desired features for promising device applications.

ACKNOWLEDGMENTS

[1] Jaeki Jeong *et al.*, Pseudo-halide anion engineering for α-FAPbI$_3$ perovskite solar cells, Nature **592**, 381 (2021).

[2] Leqi Li, Xin Liu, Hongjian Zhang, Binbin Zhang, Wanqi Jie, Paul J. Sellin, Chuanhao Hu, Guoqiang Zeng, and Yadong Xu, Enhanced X-ray sensitivity of MAPbBr$_3$ detector by tailoring the interface-states density, ACS Appl. Mater. Interfaces **11**, 7522 (2019).

[3] Junyi Huang, Chen Dong, Yantao Mei, Xiayao Lu, Gentian Yue, Yueyue Gao, Rong Liu, Weifeng Zhang, and Furui Tan, The precursor-compensation strategy boosts the photoresponse performance of air-stable, self-powered Cs$_2$SnI$_6$ photodetectors, J. Mater. Chem. C **9**, 14217 (2021).

[4] Zhenzhen Zhang, Yongqi Liang, Hanlin Huang, Xingyi Liu, Qi Li, and Langxing Chen, and Dongsheng Xu, Stable and highly efficient photocatalysis with lead-free double-perovskite of Cs$_2$AgBiBr$_6$, Angew. Chem., Int. Ed. **58**, 7263 (2019).

[5] Hang Yin, Junsheng Chen, Peng Guan, Daoyuan Zheng, Qingkun Kong, Songqiu Yang, Panwang Zhou, Bin Yang, Tönu Pullerits, and Keli Han, Controlling photoluminescence and photocatalysis activities in lead-free Cs$_2$Pt$_x$Sn$_{1-x}$Cl$_6$ perovskites via ion substitution, Angew. Chem. **133**, 22875 (2021).

[6] Weidong Xu *et al.*, Rational molecular passivation for high-performance perovskite light-emitting diodes, Nat. Photonics **13**, 418 (2019).

[7] Jieyuan Cui, Yang Liu, Yunzhou Deng, Chen Lin, Zhishan Fang, Chensheng Xiang, Peng Bai, Kai Du, Xiaobing Zuo, Kaichuan Wen, Shaolong Gong, Haiping He, Zhizhen Ye, Yunan Gao, He Tian, Baodan Zhao, Jianpu Wang, and Yizheng Jin, Efficient light-emitting diodes based on oriented perovskite nanoplatelets, Sci. Adv. **7**, eabg8458 (2021).

[8] Yen-Hung Lin *et al.*, A piperidinium salt stabilizes efficient metal-halide perovskite solar cells, Science **369**, 96 (2020).

[9] Martin Stolterfoht, Christian M. Wolff, José A. Márquez, Shanshan Zhang, Charles J. Hages, Daniel Rothhardt, Steve Albrecht, Paul L. Burn, Paul Meredith, Thomas Unold, and Dieter Neher, Visualization and suppression of interfacial recombination for high-efficiency large-area pin perovskite solar cells, Nat. Energy **3**, 847 (2018).

[10] Feliciano Giustino and Henry J. Snaith, Toward lead-free perovskite solar cells, ACS Energy Lett. **1**, 1233 (2016).

[11] Shuyan Shao, Jian Liu, Giuseppe Portale, Hong-Hua Fang, Graeme R. Blake, Gert H. ten Brink, L. Jan Anton Koster, and Maria Antonietta Loi, Highly reproducible Sn-based hybrid perovskite solar cells with 9% efficiency, Adv. Energy Mater. **8**, 1702019 (2018).

[12] Jiban Kangsabanik, Supriti Ghorui, M. Aslam, and Aftab Alam, Optoelectronic properties and defect physics of lead-free photovoltaic absorbers Cs$_2$Au^{I}Au$^{III}X_6$ (X = I, Br), Phys. Rev. Appl. **13**, 014005 (2020).

[13] Constantinos C. Stoumpos, Christos D. Malliakas, and Mercouri G. Kanatzidis, Semiconducting tin and lead iodide perovskites with organic cations: Phase transitions, high mobilities, and near-infrared photoluminescent properties, Inorg. Chem. **52**, 9019 (2013).

[14] Xin-Gang Zhao, Ji-Hui Yang, Yuhao Fu, Dongwen Yang, Qiaoling Xu, Liping Yu, Su-Huai Wei, and Lijun Zhang, Design of lead-free inorganic halide perovskites for solar cells via cation-transmutation, J. Am. Chem. Soc. **139,** 2630 (2017).

[15] Mengling Xia, Jun-Hui Yuan, Guangda Niu, Xinyuan Du, Lixiao Yin, Weicheng Pan, Jiajun Luo, Zhigang Li, Hong-tao Zhao, Kan-Hao Xue, Xiangshui Miao, and Jiang Tang, Unveiling the structural descriptor of $A_3B_2X_9$ perovskite derivatives toward X-ray detectors with low detection limit and high stability, Adv. Funct. Mater. **30,** 1910648 (2020).

[16] Yao Cai, Wei Xie, Hong Ding, Yan Chen, Krishnamoorthy Thirumal, Lydia H. Wong, Nripan Mathews, Subodh G. Mhaisalkar, Matthew Sherburne, and Mark Asta, Computational study of halide perovskite-derived A_2BX_6 inorganic compounds: Chemical trends in electronic structure and structural stability, Chem. Mater. **29,** 7740 (2017).

[17] George Volonakis, Marina R. Filip, Amir Abbas Haghighirad, Nobuya Sakai, Bernard Wenger, Henry J. Snaith, and Feliciano Giustino, Lead-free halide double perovskites via heterovalent substitution of noble metals, J. Phys. Chem. Lett. **7,** 1254 (2016).

[18] Adam H. Slavney, Te Hu, Aaron M. Lindenberg, and Hemamala I. Karunadasa, A bismuth-halide double perovskite with long carrier recombination lifetime for photovoltaic applications, J. Am. Chem. Soc. **138,** 2138 (2016).

[19] Jiban Kangsabanik, Vipinraj Sugathan, Anuradha Yadav, Aswani Yella, and Aftab Alam, Double perovskites overtaking the single perovskites: A set of new solar harvesting materials with much higher stability and efficiency, Phys. Rev. Mater. **2,** 055401 (2018).

[20] George Volonakis, Amir Abbas Haghighirad, Rebecca L. Milot, Weng H. Sio, Marina R. Filip, Bernard Wenger, Michael B. Johnston, Laura M. Herz, Henry J. Snaith, and Feliciano Giustino, $Cs_2InAgCl_6$: A new lead-free halide double perovskite with direct band gap, J. Phys. Chem. Lett. **8,** 772 (2017).

[21] Fan Bai, Yonghong Hu, Yanqiang Hu, Ting Qiu, Xiaoliang Miao, and Shufang Zhang, Lead-free, air-stable ultrathin $Cs_3Bi_2I_9$ perovskite nanosheets for solar cellss, Solar Energy Mater. Solar Cells **184,** 15 (2018).

[22] Anupriya Singh, Karunakara Moorthy Boopathi, Anisha Mohapatra, Yang Fang Chen, Gang Li, Chih Wei Chu, Photovoltaic performance of vapor-assisted solution-processed layer polymorph of $Cs_3Sb_2I_9$, ACS Appl. Mater. Interfaces **10,** 2566 (2018).

[23] Xiaofeng Qiu, Bingqiang Cao, Shuai Yuan, Xiangfeng Chen, Zhiwen Qiu, Yanan Jiang, Qian Ye, Hongqiang Wang, Haibo Zeng, Jian Liu, and Mercouri G. Kanatzidis, From unstable $CsSnI_3$ to air-stable Cs_2SnI_6: A lead-free perovskite solar cell light absorber with bandgap of 1.48 eV and high absorption coefficient, Solar Energy Mater. Solar Cells **159,** 227 (2017).

[24] Ming-Gang Ju, Min Chen, Yuanyuan Zhou, Hector F. Garces, Jun Dai, Liang Ma, Nitin P. Padture, and Xiao Cheng Zeng, Earth-abundant nontoxic titanium (IV)-based vacancy-ordered double perovskite halides with tunable 1.0 to 1.8 eV bandgaps for photovoltaic applications, ACS Energy Lett. **3,** 297 (2018).

[25] Byunghong Lee, Anthony Krenselewski, Sung Il Baik, David N. Seidman, and Robert P. H. Chang, Solution processing of air-stable molecular semiconducting iodosalts, $Cs_2SnI_{6-x}Br_x$, for potential solar cell applications, Sustainable Energy Fuels **1,** 710 (2017).

[26] Dali Shao, Weiguang Zhu, Guoqing Xin, Xueqing Liu, Tianmeng Wang, Sufei Shi, Jie Lian, and Shayla Sawyer, A high performance UV–visible dual-band photodetector based on an inorganic Cs_2SnI_6 perovskite/ZnO heterojunction structure, J. Mater. Chem. C **8,** 1819 (2020).

[27] Byunghong Lee, Constantinos C. Stoumpos, Nanjia Zhou, Feng Hao, Christos Malliakas, Chen-Yu Yeh, Tobin J. Marks, Mercouri G. Kanatzidis, and Robert P. H. Chang, Air-stable molecular semiconducting iodosalts for solar cell applications: Cs_2SnI_6 as a hole conductor, J. Am. Chem. Soc. **136,** 15379 (2014).

[28] Annalise E. Maughan, Alex M. Ganose, Mitchell M. Bordelon, Elisa M. Miller, David O. Scanlon, and James R. Neilson, Defect tolerance to intolerance in the vacancy-ordered double perovskite semiconductors Cs_2SnI_6 and Cs_2TeI_6, J. Am. Chem. Soc. **138,** 8453 (2016).

[29] Bayrammurad Saparov, Jon-Paul Sun, Weiwei Meng, Zewen Xiao, Hsin-Sheng Duan, Oki Gunawan, Donghyeop Shin, Ian G. Hill, Yanfa Yan, and David B. Mitzi, Thin-film deposition and characterization of a Sn-deficient perovskite derivative Cs_2SnI_6, Chem. Mater. **28,** 2315 (2016).

[30] Eduardo López-Fraguas, Sofia Masi, and Ivan Mora-Sero, Optical characterization of lead-free Cs_2SnI_6 double perovskite fabricated from degraded and reconstructed $CsSnI_3$ films, ACS Appl. Energy Mater. **2,** 8381 (2019).

[31] Fawen Guo, Zonghuan Lu, Dibyajyoti Mohanty, Tianmeng Wang, Ishwara B. Bhat, Shengbai Zhang, Sufei Shi, Morris A. Washington, Gwo-Ching Wang, and Toh-Ming Lu, A two-step dry process for Cs_2SnI_6 perovskite thin film, Mater. Res. Lett. **5,** 540 (2017).

[32] Annalise E. Maughan, Alex M. Ganose, Andrew M. Candia, Juliette T. Granger, David O. Scanlon, and James R. Neilson, Anharmonicity and octahedral tilting in hybrid vacancy-ordered double perovskites, Chem. Mater. **30,** 472 (2018).

[33] Preeti Bhumla, Manjari Jain, Sajjan Sheoran, and Saswata Bhattacharya, Vacancy-ordered double perovskites Cs_2BI_6 (B = Pt, Pd, Te, Sn): An emerging class of thermoelectric materials, J. Phys. Chem. Lett. **13,** 11655 (2022).

[34] Zhifang Tan, Yanmeng Chu, Jinxi Chen, Jinghui Li, Guoqi Ji, Guangda Niu, Liang Gao, Zewen Xiao, and Jiang Tang, Lead-free perovskite variant solid solutions $Cs_2Sn_{1-x}Te_xCl_6$: Bright luminescence and high anti-water stability, Adv. Mater. **32,** 2002443 (2020).

[35] Isabel Vazquez-Fernandez, Silvia Mariotti, Oliver S. Hutter, Max Birkett, Tim D. Veal, Theodore D. C. Hobson, Laurie J. Phillips, Lefteris Danos, Pabitra K. Nayak, Henry J. Snaith, Wei Xie, Matthew P. Sherburne, Mark Asta, and Ken Durose, Vacancy-ordered double perovskite Cs_2TeI_6 thin films for optoelectronics, Chem. Mater. **32,** 6676 (2020).

[36] Dakota Schwartz, Rubaiya Murshed, Harry Larson, Benedikt Usprung, Sina Soltanmohamad, Ramesh Pandey,

Edward S. Barnard, Angus Rockett, Thomas Hartmann, Ivano E. Castelli, and Shubhra Bansal, Air stable, high-efficiency, Pt-based halide perovskite solar cells with long carrier lifetimes, Phys. Status Solidi (RRL)–Rapid Research Letters **14**, 2000182 (2020).

[37] Min Chen, Ming-Gang Ju, Alexander D. Carl, Yingxia Zong, Ronald L. Grimm, Jiajun Gu, Xiao Cheng Zeng, Yuanyuan Zhou, and Nitin P. Padture, Cesium titanium (IV) bromide thin films based stable lead-free perovskite solar cells, Joule **2**, 558 (2018).

[38] Nobuya Sakai, Amir Abbas Haghighirad, Marina R. Filip, Pabitra K. Nayak, Simantini Nayak, Alexandra Ramadan, Zhiping Wang, Feliciano Giustino, and Henry J. Snaith, Solution-processed cesium hexabromopalladate (IV), Cs_2PdBr_6, for optoelectronic applications, J. Am. Chem. Soc. **139**, 6030 (2017).

[39] Anna Abfalterer, Javad Shamsi, Dominik J. Kubicki, Christopher N. Savory, James Xiao, Giorgio Divitini, Wei-wei Li, Stuart Macpherson, Krzysztof Gałkowski, Judith L. MacManus-Driscoll, David O. Scanlon, and Samuel D. Stranks, Colloidal synthesis and optical properties of perovskite-inspired cesium zirconium halide nanocrystals, ACS Mater. Lett. **2**, 1644 (2020).

[40] W. Kohn and L. J. Sham, Self-consistent equations including exchange and correlation effects, Phys. Rev. **140**, A1133 (1965).

[41] Peter E. Blöchl, Projector augmented-wave method, Phys. Rev. B **50**, 17953 (1994).

[42] G. Kresse and D. Joubert, From ultrasoft pseudopotentials to the projector augmented-wave method, Phys. Rev. B **59**, 1758 (1999).

[43] Georg Kresse and Jürgen Hafner, *Ab initio* molecular dynamics for liquid metals, Phys. Rev. B **47**, 558 (1993).

[44] Georg Kresse and Jürgen Hafner, *Ab initio* molecular-dynamics simulation of the liquid-metal–amorphous-semiconductor transition in germanium, Phys. Rev. B **49**, 14251 (1994).

[45] Georg Kresse and Jürgen Furthmüller, Efficient iterative schemes for *ab initio* total-energy calculations using a plane-wave basis set, Phys. Rev. B **54**, 11169 (1996).

[46] G. Kresse and J. Furthmüller, Efficiency of ab-initio total energy calculations for metals and semiconductors using a plane-wave basis set, Comput. Mater. Sci. **6**, 15 (1996).

[47] John P. Perdew, Kieron Burke, and Matthias Ernzerhof, Generalized Gradient Approximation Made Simple, Phys. Rev. Lett. **77**, 3865 (1996).

[48] Aliaksandr V. Krukau, Oleg A. Vydrov, Artur F. Izmaylov, and Gustavo E. Scuseria, Influence of the exchange screening parameter on the performance of screened hybrid functionals, J. Chem. Phys. **125**, 224106 (2006).

[49] N. Hatada, Chesta. Available at http://www.aqua.mtl.kyoto-u.ac.jp/chestaEng.html (2010).

[50] Fredrik Eriksson, Erik Fransson, and Paul Erhart, The Hiphive package for the extraction of high-order force constants by machine learning, Adv. Theory Simul. **2**, 1800184 (2019).

[51] Alex M. Ganose, Junsoo Park, Alireza Faghaninia, Rachel Woods-Robinson, Kristin A. Persson, and Anubhav Jain,

Efficient calculation of carrier scattering rates from first principles, Nat. Commun. **12**, 2222 (2021).

[52] Jarvist Moore Frost, Calculating polaron mobility in halide perovskites, Phys. Rev. B **96**, 195202 (2017).

[53] Robert W. Hellwarth and Ivan Biaggio, Mobility of an electron in a multimode polar lattice, Phys. Rev. B **60**, 299 (1999).

[54] Jens Jørgen Mortensen, Lars Bruno Hansen, and Karsten Wedel Jacobsen, Real-space grid implementation of the projector augmented wave method, Phys. Rev. B **71**, 035109 (2005).

[55] Jussi Enkovaara *et al.*, Electronic structure calculations with GPAW: A real-space implementation of the projector augmented-wave method, J. Phys.: Condens. Matter **22**, 253202 (2010).

[56] Ask Hjorth Larsen *et al.*, The atomic simulation environment–A Python library for working with atoms, J. Phys.: Condens. Matter **29**, 273002 (2017).

[57] Jiban Kangsabanik, Mark Kamper Svendsen, Alireza Taghizadeh, Andrea Crovetto, and Kristian S. Thygesen, Indirect band gap semiconductors for thin-film photovoltaics: High-throughput calculation of phonon-assisted absorption, J. Am. Chem. Soc. **144**, 19872 (2022).

[58] See the Supplemental Material http://link.aps.org/supplemental/10.1103/PhysRevApplied.21.024036, which contains details about different further structural properties, stability, further electronic structure data, transition probabilities, further optical data, and transport-related properties. It contains a brief discussion about SLME, which can also be found in refs. [87,100–102].

[59] Andreas Kaltzoglou, Maria Antoniadou, Athanassios G. Kontos, Constantinos C. Stoumpos, Dorothea Perganti, Eirini Siranidi, Vasilios Raptis, Kalliopi Trohidou, Vassilis Psycharis, Mercouri G. Kanatzidis, and Polycarpos Falaras, Optical-vibrational properties of the Cs_2SnX_6 (X = Cl, Br, I) defect perovskites and hole-transport efficiency in dye-sensitized solar cells, J. Phys. Chem. C **120**, 11777 (2016).

[60] Huaping Peng, Luyao Xu, Yilun Sheng, Weiming Sun, Yu Yang, Haohua Deng, Wei Chen, and Juewen Liu, Highly conductive ligand-free Cs_2PtBr_6 perovskite nanocrystals with a narrow bandgap and efficient photoelectrochemical performance, Small **17**, 2102149 (2021).

[61] Julie Euvrard, Xiaoming Wang, Tianyang Li, and Yanfa Yan, and David B. Mitzi, Is Cs_2TiBr_6 a promising Pb-free perovskite for solar energy applications?, J. Mater. Chem. A **8**, 4049 (2020).

[62] Wu Li, Electrical transport limited by electron-phonon coupling from Boltzmann transport equation: An *ab initio* study of Si, Al, and MoS_2, Phys. Rev. B **92**, 075405 (2015).

[63] Samuel Poncé, Wenbin Li, Sven Reichardt, and Feliciano Giustino, First-principles calculations of charge carrier mobility and conductivity in bulk semiconductors and two-dimensional materials, Rep. Prog. Phys. **83**, 036501 (2020).

[64] Mark Lundstrom, in *Fundamentals of Carrier Transport*, 2nd ed. (Cambridge University Press, 2010).

[65] Samuel Poncé, Elena R. Margine, and Feliciano Giustino, Towards predictive many-body calculations of

phonon-limited carrier mobilities in semiconductors, Phys. Rev. B **97**, 121201 (2018).

[66] Lei Zhou, Jin-Feng Liao, Zeng-Guang Huang, Xu-Dong Wang, Yang-Fan Xu, Hong-Yan Chen, Dai-Bin Kuang, and Cheng-Yong Su, All-inorganic lead-free Cs_2PdX_6 (X = Br, I) perovskite nanocrystals with single unit cell thickness and high stability, ACS Energy Lett. **3**, 2613 (2018).

[67] Alexander E. Fedorovskiy, Nikita A. Drigo, and Mohammad Khaja Nazeeruddin, The role of Goldschmidt's tolerance factor in the formation of A_2BX_6 double halide perovskites and its optimal range, Small Methods **4**, 1900426 (2020).

[68] Guenter Bergerhoff, R. Hundt, R. Sievers, and I. D. Brown, The inorganic crystal structure data base, J. Chem. Inf. Comput. Sci. **23**, 66 (1983).

[69] Inorganic Crystal Structure Database (ICSD) https://icsd.fiz-karlsruhe.de.

[70] Scott Kirklin, James E. Saal, Bryce Meredig, Alex Thompson, Jeff W. Doak, Muratahan Aykol, Stephan Rühl, and Chris Wolverton, The Open Quantum Materials Database (OQMD): Assessing the accuracy of DFT formation energies, Npj Comput. Mater. **1**, 1 (2015).

[71] James E. Saal, Scott Kirklin, Muratahan Aykol, Bryce Meredig, and Christopher Wolverton, Materials design and discovery with high-throughput density functional theory: The Open Quantum Materials Database (OQMD), Jom **65**, 1501 (2013).

[72] Anubhav Jain, Shyue Ping Ong, Geoffroy Hautier, Wei Chen, William Davidson Richards, Stephen Dacek, Shreyas Cholia, Dan Gunter, David Skinner, Gerbrand Ceder, and Kristin A. Persson, Commentary: The Materials Project: A materials genome approach to accelerating materials innovation, APL Mater. **1**, 011002 (2013).

[73] Animesh Bhui, Tanmoy Ghosh, Koushik Pal, Kewal Singh Rana, Kaushik Kundu, Ajay Soni, and Kanishka Biswas, Intrinsically low thermal conductivity in the *n*-type vacancy-ordered double perovskite Cs_2SnI_6: Octahedral rotation and anharmonic rattling, Chem. Mater. **34**, 3301 (2022).

[74] Un-Gi Jong, Chol-Jun Yu, Yun-Hyok Kye, Song-Hyok Choe, Jin-Song Kim, and Yong-Guk Choe, Anharmonic phonons and phase transitions in the vacancy-ordered double perovskite Cs_2SNi_6 from first-principles predictions, Phys. Rev. B **99**, 184105 (2019).

[75] Bruno Cucco, Claudine Katan, Jacky Even, Mikaël Kepenekian, and George Volonakis, Fine structure of excitons in vacancy-ordered halide double perovskites, ACS Mater. Lett. **5**, 52 (2022).

[76] Shanti Maria Liga and Gerasimos Konstantatos, Colloidal synthesis of lead-free $Cs_2TiBr_{6-x}I_x$ perovskite nanocrystals, J. Mater. Chem. C **9**, 11098 (2021).

[77] John. S Townsend, *A Modern Approach to Quantum Mechanicss* (University Science Books, Claremont, CA, USA, 2012).

[78] Bruno Cucco, Gaëlle Bouder, Laurent Pedesseau, Claudine Katan, Jacky Even, Mikael Kepenekian, and George Volonakis, Electronic structure and stability of Cs_2TiX_6 and Cs_2ZrX_6 (X = Br, I) vacancy ordered double perovskites, Appl. Phys. Lett. **119**, 181903 (2021).

[79] Muhammed Hamdan and Aravind Kumar Chandiran, Cs_2PtI_6 halide perovskite is stable to air, moisture, and extreme pH: Application to photoelectrochemical solar water oxidation, Angew. Chem. **132**, 16167 (2020).

[80] Shuzhang Yang, Liang Wang, Shuai Zhao, Anmin Liu, Yi Zhou, Qianji Han, Fengyang Yu, Liguo Gao, Chu Zhang, and Tingli Ma, Novel lead-free material Cs_2PtI_6 with narrow bandgap and ultra-stability for its photovoltaic application, ACS Appl. Mater. Interfaces **12**, 44700 (2020).

[81] Jin Zhang, Chunhui Yu, Lili Wang, Yizhi Li, Yuhang Ren, and Kai Shum, Energy barrier at the N719-dye/$CsSnI_3$ interface for photogenerated holes in dye-sensitized solar cells, Sci. Rep. **4**, 6954 (2014).

[82] Seán R. Kavanagh, Christopher N. Savory, Shanti M. Liga, Gerasimos Konstantatos, Aron Walsh, and David O. Scanlon, Frenkel excitons in vacancy-ordered titanium halide perovskites (Cs_2TiX_6), J. Phys. Chem. Lett. **13**, 10965 (2022).

[83] Shanti M. Liga, Seán R. Kavanagh, Aron Walsh, David O. Scanlon, and Gerasimos Konstantatos, Mixed-cation vacancy-ordered perovskites ($Cs_2Ti_{1-x}Sn_xX_6$; X = I or Br): Low-temperature miscibility, additivity, and tunable stability, J. Phys. Chem. C **127**, 21399 (2023).

[84] Andreas Weu, Thomas R. Hopper, Vincent Lami, Joshua A. Kreß, Artem A. Bakulin, and Yana Vaynzof, Field-assisted exciton dissociation in highly efficient PffBT4T-2OD:fullerene organic solar cells, Chem. Mater. **30**, 2660 (2018).

[85] Li-Min Chen, Zheng Xu, Ziruo Hong, and Yang Yang, Interface investigation and engineering–achieving high performance polymer photovoltaic devices, J. Mater. Chem. **20**, 2575 (2010).

[86] Ni Zhao, Tim P. Osedach, Liang-Yi Chang, Scott M. Geyer, Darcy Wanger, Maddalena T. Binda, Alexi C. Arango, Moungi G. Bawendi, and Vladimir Bulovic, Colloidal PbS quantum dot solar cells with high fill factor, ACS Nano **4**, 3743 (2010).

[87] Liping Yu and Alex Zunger, Identification of Potential Photovoltaic Absorbers Based on First-Principles Spectroscopic Screening of Materials, Phys. Rev. Lett. **108**, 068701 (2012).

[88] Su-Huai Wei, Overcoming the doping bottleneck in semiconductors, Comput. Mater. Sci. **30**, 337 (2004).

[89] Thomas Kirchartz, Julian Mattheis, and Uwe Rau, Detailed balance theory of excitonic and bulk heterojunction solar cells, Phys. Rev. B **78**, 235320 (2008).

[90] Adair Nicolson, Seán R. Kavanagh, Christopher N. Savory, Graeme W. Watson, and David O. Scanlon, Cu_2SiSe_3 as a promising solar absorber: Harnessing cation dissimilarity to avoid killer antisites, J. Mater. Chem. A **11**, 14833 (2023).

[91] Julian FRV Silveira, Rafael Besse, Alexandre Cavalheiro Dias, Naidel AMS Caturello, and Juarez L. F. Da Silva, Tailoring excitonic and optoelectronic properties of transition metal dichalcogenide bilayers, J. Phys. Chem. C **126**, 9173 (2022).

[92] Annalise E. Maughan, Alex M. Ganose, Mohammed A. Almaker, David O. Scanlon, and James R. Neilson, Tolerance factor and cooperative tilting effects in

vacancy-ordered double perovskite halides, Chem. Mater. **30**, 3909 (2018).

[93] Lewis A. D. Irvine, Alison B. Walker, and Matthew J. Wolf, Quantifying polaronic effects on the scattering and mobility of charge carriers in lead halide perovskites, Phys. Rev. B **103**, L220305 (2021).

[94] Richard Phillips Feynman, Slow electrons in a polar crystal, Phys. Rev. **97**, 660 (1955).

[95] Jozef T. Devreese and Alexandre S. Alexandrov, Fröhlich polaron and bipolaron: Recent developments, Rep. Prog. Phys. **72**, 066501 (2009).

[96] Weng Hong Sio, Carla Verdi, Samuel Poncé, and Feliciano Giustino, *Ab initio* theory of polarons: Formalism and applications, Phys. Rev. B **99**, 235139 (2019).

[97] Debjit Manna, Jiban Kangsabanik, Tapan Kumar Das, Debashish Das, Aftab Alam, and Aswani Yella, Lattice dynamics and electron–phonon coupling in lead-free $Cs_2AgIn_{1-x}Bi_xCl_6$ double perovskite nanocrystals, J. Phys. Chem. Lett. **11**, 2113 (2020).

[98] Rishabh Saxena, Jiban Kangsabanik, Ayush Kumar, Aga Shahee, Shivam Singh, Nakul Jain, Supriti Ghorui, Vinod Kumar, Avinash V. Mahajan, Aftab Alam, and Dinesh Kabra, Contrasting temperature dependence of the band gap in $CH_3NH_3PbX_3$ (X = I, Br, Cl): Insight from lattice dilation and electron-phonon coupling, Phys. Rev. B **102**, 081201 (2020).

[99] Christian Fey, Peter Schmelcher, Atac Imamoglu, and Richard Schmidt, Theory of exciton-electron scattering in atomically thin semiconductors, Phys. Rev. B **101**, 195417 (2020).

[100] William Shockley and Hans J. Queisser, Detailed balance limit of efficiency of p-n junction solar cells, J. Appl. Phys. **32**, 510 (1961).

[101] Martin A. Green, Third generation photovoltaics: Advanced solar energy conversion, Phys. Today **57**, 71 (2004).

[102] T. O. M Tiedje, E. L. I Yablonovitch, George D Cody, and Bonnie G Brooks, Limiting efficiency of silicon solar cells, IEEE Trans. Electron Devices **31**, 711 (1984).